C. R. Mecanique 345 (2017) 317–328

Contents lists available at ScienceDirect

Comptes Rendus Mecanique

www.sciencedirect.com

Modeling of failure characteristics of rectangular hard rock influenced by sample height-to-width ratios: A finite/discrete element approach

Fan Feng *, Xibing Li, Diyuan Li

School of Resources and Safety Engineering, Central South University, Changsha, Hunan Province 410083, China

ARTICLE INFO

Article history:
Received 23 November 2016
Accepted 2 March 2017
Available online 18 March 2017

Keywords:
Finite/discrete element approach
Sample height-to-width ratios
Slabbing failure
Shear failure
Extension meso-cracks
Hard rock

ABSTRACT

In the present study, a combined finite/element approach is used to analyze failure characteristics of a rectangular hard rock with different sample height-to-width ratios based on the uniaxial compression test. The objective of this paper is to illustrate the transitional mechanisms from shear fracture to extension failure of brittle rocks and the occurrence conditions of surface-parallel slabbing. Numerical results show that failure modes have experienced the shear, tension with shear and surface-parallel slabbing failure with the decrease of sample height-to-width ratios. It is seen from the simulation results that the shear band in larger height-to-width ratios is composed of an amount of extension meso-cracks that are parallel to the loading direction, and the slabbing failure tends to be the result of the accessible propagation of extension meso-cracks due to short sample height, which validate the essence of extension failure in hard rocks. The good agreement between simulation and laboratory testing also shows the practicability and advancement of a combined finite/discrete element approach.

1. Introduction

With the increasing demand for mineral resources and gradual consumption of shallow resources, more and more metal mines are deeper and deeper. It seems that hard rocks may have extremely distinct mechanical behavior compared to that in shallow geological conditions; surface-parallel slabbing failure is the dominant and prevailing phenomenon for deep highly-stressed hard rocks [1].

Generally speaking, extension fracture and shear fracture, which have been studied by numerous researchers in the laboratory, are the two main failure modes for hard rocks [2,3]. The failure modes loaded in uniaxial compression test under the laboratory conditions are divided into splitting failure and shear failure [4]. In the early 1960s, people began to concentrate on the axial cleavage failure of rocks under the condition of compression load [5]. Such failure mode is not only related to the loading regime, stress condition and degree of brittleness of rocks, but also related to the propagation of extension cracks in rock specimen. The empirical Mohr–Coulomb and Hoek–Brown criteria are applicable for shear failure in rock mechanics, so these criteria may not be suitable for analyzing the mechanical behavior in terms of slabbing or splitting failure. Griffth's theory highlights the importance of the flaws in brittle materials. Under the condition of complex

* Corresponding author.
E-mail address: 155501006@csu.edu.cn (F. Feng).

http://dx.doi.org/10.1016/j.crme.2017.03.001
1631-0721/

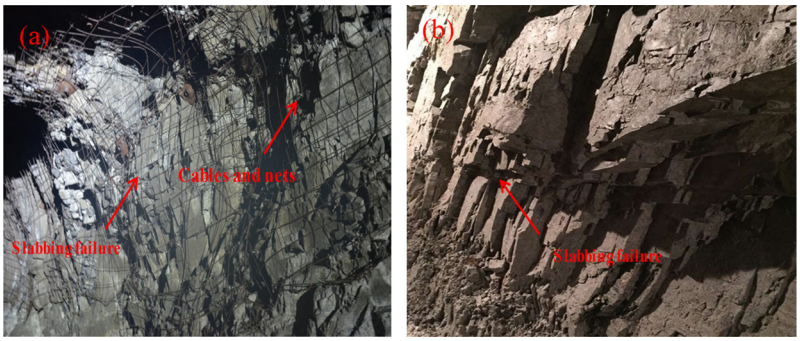

Fig. 1. Slabbing failure and slab buckling rock burst in the 640 level of Maluping mine. (a) Phosphate rock in the stope and (b) dolomite in the level drive.

stress, these flaws and defects will generate tensile meso-cracks, which result finally in brittle tensile failure. Li et al. [6] found that in specimens with larger height-to-width ratios loaded in uniaxial compression test, a great number of extension meso-cracks parallel to the loading direction took place, which finally coalesced together to form a shear band. This failure phenomenon is quite similar to Brace's experimental results [7]. Nevertheless, the hypothesis according to which extension failure is the failure mechanism of brittle-hard rocks still needs further validation and illustration by means of various methods, such as numerical approach.

The uniaxial compression test has been a conventional one in evaluating the intact and hard rock strength and failure mode. Wawersik and Fairhurst [8] conducted some compressive tests on rock specimens using a stiff loading machine and concluded that failure in uniaxial compression of rock can occur in two modes. Fakhimi and Hemami [9] used the bonded particle discrete element method and experimental test to analyze the influence of the stiffness of the loading machine on uniaxial compression. As a consequence of axial and radial cracks, rock pieces in the form of cantilever beams are generated around the specimen free surface, the final failure mode being splitting failure. Reference [6] analyzed the failure characteristics of rectangular prismatic samples of hard rock, and found out that the failure mode of hard rock may be transformed from shear to slabbing when the height/width ratio of the prism specimen is 0.5 under uniaxial compression. Freddi and Royer-Carfagni [10] used a fracture mechanics model together with some heterogeneous inclusions within the compressively loaded specimens to model the axial splitting. Wen et al. [11] studied the influence of different height to diameter ratio on the acoustic emission characteristics of coal rock damage evolution using a microparticle flow PFC^{2D} software platform.

In conclusion, an extensive experimental and numerical research has been carried out for the uniaxial compression test. In-depth study of uniaxial compressive test for hard rocks can also help us understand the failure of pillars in deep mining and tunneling projects. According to Ortlepp's description [12], spalling or slabbing is generally defined as the formation of stress-induced slabs on the boundary of an underground excavation. It initiates in the region of maximum tangential stresses and results in a V-shaped notch that is local to the boundary of the opening. Reference [9] found that higher friction coefficient of pillar-roof interface and enough pillar stiffness can result in tensile splitting failure at the pillar ends. Martin and Maybee [13] observed that the dominant failure mode was progressive slabbing and spalling rather than shear in pillars of some Canadian hard rock mines. In addition to the hard rock pillars, the slabbing and spalling failure can be observed near the tunnel surface and excavation boundaries. The author also observed slabbing failure (seen in Fig. 1) of two typical hard rocks (dolomite and phosphate rock) in Maluping mine, Guiyang Province, China, and recommended that the increase of intermediate principle stress not only promotes the formation of slabbing, but also intensifies the possibility of slab buckling rock burst.

Many researchers employ numerical approaches to study the progressive failure of rock and rock-like materials [14]. During the fracturing processes, the rock has transformed from a stable continuum into a fractured discontinuum due to crack initiation, propagation, and coalescence. Recently, the FEM/DEM combined method, which integrates the FEM and DEM into a single tool, has provided a unified framework for both continuous and discontinuous problems [15]. The numerical results showed good agreement between the final fracture patterns obtained during 2D and 3D simulations. In the present study, a FEM/DEM combined approach (ELFEN, Rockfield Software Ltd.) is adopted to simulate the fracture process of rectangular hard rock samples in uniaxial compression test, with particularly attention paid to the consideration of different height-to-width ratios. A typical hard rock type based on Iddefjord granite is selected for the numerical simulation. The purpose of this paper is to reveal the transitional mechanisms from shear fracture to extension failure of brittle rocks and the occurrence conditions of surface-parallel slabbing. Numerical results based on FEM/DEM show good agreement with the experimental results, which would provide a reasonable and functional way to study various rock mechanics and rock engineering problems.

2. Fundamental principles of the finite/discrete element approach

The combined finite/discrete approach is a numerical method that combines continuum mechanical principles with discontinuum algorithms to simulate multiple interacting deformable solids [16]. It was proposed by Munjiza [17], who takes

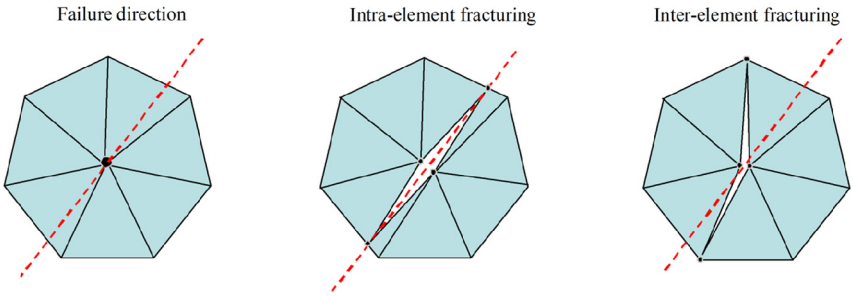

Fig. 2. ELFEN crack insertion procedure (modified after Cai [15]).

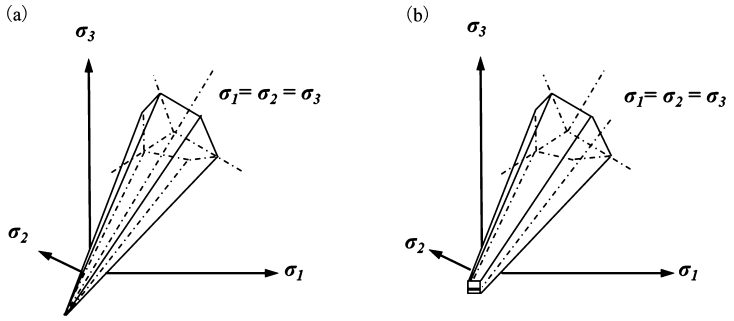

Fig. 3. The conical nature of the yield surface of (a) conventional M–C tensile yield surface and (b) M–C with Rankine tensile corner (modified after Hamdi et al. [22]).

advantage of both techniques and to combine the FEM and DEM into a hybrid finite/discrete modeling methodology. In FEM/DEM, each discrete element is discretized into finite elements, so transition from continuum to discontinuum is done through a fracture and fragmentation process. In this paper, ELFEN, which contains a variety of constitutive models and is capable of both explicit and implicit analyzes in 2D and 3D types, was used to simulate the failure characteristics of hard rock during uniaxial compression. If the failure criterion within the intact rock (initially represented as a FEM domain) is met, then a crack is initiated. An obvious distinction from other numerical codes is its ability to allow the new cracks to cut across the original mesh (intra-element fracturing) rather than along or around the element boundary (inter-element fracturing) merely, as it can be seen in Fig. 2. Whether the fractures split the elements is determined by the value for "Smallest Element" set under the discrete contact parameters. If this value is the same as or larger than the original mesh size, the fractures will propagate along the element boundaries only, as the minimum size has already been reached. If it is smaller than the original mesh, the fractures may split elements, if conditions dictate. ELFEN has a large range of material modeling options that may be combined to create material models for differing classes of problems. In the present study, the Mohr–Coulomb constitutive model with rotating crack is used for the uniaxial compression test because it is able to simulate rock fracturing due to both tension and compression.

In the uniaxial compression test, the Iddefjord granite is governed by the Mohr–Coulomb constitutive model with rotating crack. This model is able to simulate rock fracturing due to both tension and compression [18]. There are five plastic material parameters: cohesion (c), friction angle (φ), dilatancy angle (ψ), tensile strength (σ_t), fracture energy (G_f). The Mohr–Coulomb yield criterion is a generalization of the Coulomb friction failure law and is defined by:

$$\tau = c - \sigma_n \tan\varphi \tag{1}$$

where τ is the magnitude of the shear stress, σ_n is the normal stress, c is the cohesion, and φ is the friction angle. In the principal stress space, the yield surface has a six-sided conical shape. The conical nature of the yield surface reflects the influence of pressure on the yield stress and the criterion is applicable to rock, concrete and soil problems. The Rankine tensile corner introduces additional yield criteria defined by:

$$\sigma_i - \sigma_t = 0 \quad i = 1, 2, 3, 4 \tag{2}$$

where σ_i refers to each principal stress and σ_t is the tensile strength. Although at present no explicit softening law is included for the tensile strength, indirect softening does result from the degradation of cohesion according to the following criterion:

$$\sigma_t \le c(1 - \sin\varphi)/\cos\varphi \tag{3}$$

The conventional Mohr–Coulomb tensile yield surface is shown in Fig. 3a. Since the Mohr–Coulomb criterion may over-estimate the tensile strength of rocks, Paul [19] introduced the concept of a tension cut-off and modified Mohr–Coulomb

criterion, as it can be seen in Fig. 3b. To model the hardening or softening behavior, the material strength parameters are defined as functions of the effective plastic strain, which is defined as

$$\varepsilon^{-p}(t) = \int_0^t \sqrt{\frac{2}{3}\left(\mathrm{d}\varepsilon_1^p \mathrm{d}\varepsilon_1^p + \mathrm{d}\varepsilon_2^p \mathrm{d}\varepsilon_2^p + \mathrm{d}\varepsilon_3^p \mathrm{d}\varepsilon_3^p\right)}\mathrm{d}t \tag{4}$$

where ε^{-p} is the effective plastic strain, ε_1^p, ε_2^p and ε_3^p are the extensional inelastic strain in the direction of maximum, intermediate and minimum principle stress, respectively. In the present study, the linearized functions are adopted. In the Mohr–Coulomb constitutive model with rotating crack, it is assumed that extensional failure can be considered the dominant factor in the brittle failure of rock [18,22]. Under the circumstance of compression, the increment of inelastic strain $\Delta\varepsilon_3^p$ in the minimum principal stress direction can be associated with tensile strength degradation (damage) in the same direction, giving

$$\sigma_{\mathrm{t}3} = \sigma_{\mathrm{t}3}\left(\varepsilon_3^p\right) \quad \text{where } \varepsilon_{3_{n+1}}^p = \varepsilon_{3_n}^p + \Delta\varepsilon_3^p \tag{5}$$

where $\sigma_{\mathrm{t}3}$ is the tensile strength in the direction of the minimum principal stress, n indicates the loading step. For the linear softening of the tensile strength, Eq. (5) can be written as

$$\sigma_{\mathrm{t}3} = \sigma_{\mathrm{t}3}\left(\varepsilon_3^p\right) = \sigma_{\mathrm{t}} - H\varepsilon_3^p \tag{6}$$

where σ_{t} is the initial tensile strength and H is the linear softening modulus. In ELFEN, H is defined as

$$H = \frac{\mathrm{d}s}{\mathrm{d}\varepsilon^p} = \frac{h_{\mathrm{c}}^{(\mathrm{e})}\sigma_{\mathrm{t}}^2}{2G_{\mathrm{f}}} \tag{7}$$

where $h_{\mathrm{c}}^{(\mathrm{e})}$ is the local element length scale (average dimension) and G_{f} is the fracture energy. Once the yield surface represented by the Mohr–Coulomb model is satisfied at the element's level, the tensile strength is updated accordingly. The fracture energy G_{f} can be defined as:

$$G = \int \sigma\,\mathrm{d}u = \int \sigma\,\varepsilon(s)\mathrm{d}s \tag{8}$$

Actually, the specific fracture energy (usually referred to as a simple 'fracture energy') G_{f} is defined as the amount of energy needed to create a continuous crack on a unit area. The fracture energy, $G_{\mathrm{f}}\mathbf{A}$, can be obtained through a simple uniaxial tensile test. The total fracture energy is the area under the load displacement curve. Note that A is the cross-sectional area of the test specimen. Integrating over a localization band width l_c for a constant slope softening model gives:

$$E^{\mathrm{T}} = -\frac{f_{\mathrm{t}}^2 l_{\mathrm{c}}}{2G_{\mathrm{f}}} \tag{9}$$

where, in the finite element context, the local control length $l_{\mathrm{c}} = f(B^{\mathrm{e}})$, where B^{e} is the area of the element, E^{T} is the tangential softening modulus. Note that the relationship between fracture toughness in mode I and fracture energy can be defined as:

$$G_{\mathrm{f}} = \frac{K_{\mathrm{Ic}}^2}{E} \tag{10}$$

where K_{Ic}^2 is the fracture toughness in mode I, E is the initial Young modulus.

The Rankine rotating crack constitutive model is suitable for modeling the tensile failure of brittle materials, e.g., rock, ceramic, glass. The most important parameters in the Rankine rotating fracture model are the fracture energy and the tensile strength. The failure mechanism of brittle rocks is dominated by the formation of tensile cracks (Mode I) when tensile stress exceeds the tensile strength of the material. A detailed description of Rankine's rotating crack constitutive model could refer to Cai [15] and Hamdi et al. [22].

3. Simulation model of uniaxial compression test

The geometries of specimen and loading platens are shown in Fig. 4a. For 2D simulations, plane strain analysis in ELFEN assumes unit thickness (1 mm in the present study). Three groups of rectangular prism specimens with different height-to-width ratios based on typical hard rocks are modeled, with a constant value of the specimen's width of 50 mm, and different height values of 100, 50, and 25 mm, respectively. Here, we use the parameter λ to illustrate the height-to-width ratio of the rectangular sample for convenience, which means that λ varies from 2.0 to 0.5. Iddefjord granite is selected as the specimen material to make validation of reference [6]. The material properties for the Iddefjord granite, the loading platen and the discrete contact are listed in Table 1. The total number of unstructured triangle elements of the established models are 55,188, 37,362, and 16,120 for corresponding values of λ of 2, 1, 0.5, respectively, as it can be seen in Fig. 4b.

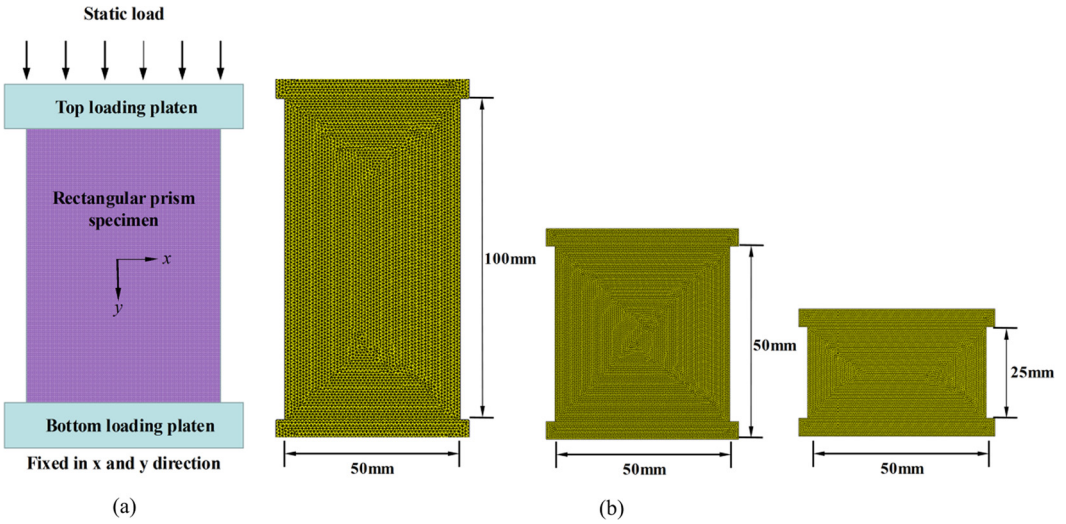

Fig. 4. (a) Model geometry of rectangular prism specimen under uniaxial compression and (b) unstructured triangle meshes of established models with different height-to-width ratios.

Table 1
Material properties in the uniaxial compression test (refer to [6]).

	Name	Iddefjord granite	Loading platen
Mechanical parameters	Young's modulus (E/GPa)	51.7	211
	Poission's ratio (μ)	0.19	0.25
	Shear modulus (G/GPa)	21.7	82
	Density (N s^2/mm^4)	2.62e−09	7.84e−09
	Uniaxial compressive strength (σ_c/MPa)	203.3	–
	Tensile strength (σ_t/MPa)	8.3	–
	Fracture energy (G_f/N/mm^2)	0.01	–
Discrete contact parameters	Normal penalty (P_n/N/mm^2)	50000	200000
	Tangential penalty (P_t/N/mm)	5000	20000
	Friction of newly generated cracks (γ)	0.5	–
	Friction between loading platens and rock specimen	0	0
	Mesh element size (mm)	0.5	0.5
	Smallest element size (mm)	0.2	0.25
	Contact type	Node-edge	Node-edge

Note: The newly generated cracks are induced by an external force that distinguish them from pre-existing flaws or faults in the rock specimens, though no pre-existing cracks were generated in the present study.

An important parameter in ELFEN is fracture energy. Models with higher fracture energy require more deformation before visible cracks are simulated, so soft rocks with ductile properties are suitable for such a case. Generally, the fracture energy values used to study quasi-brittle materials usually range from 0.01 to 0.3 N/mm [15,20]. Based on the previous evaluation and research in terms of fracture energy, the value of 0.01 N/mm is appropriate for describing its extremely hard and brittle properties for Iddefjord granite. Penalty parameters are used to evaluate the normal and tangential contact forces. The value for the normal penalty is usually in the range of $0.5E < P_n < 2.0E$, where E is Young's modulus, and the tangential penalty is about 0.1 of the normal penalty [21]. The Search Zone is used to define the area within which local nodes are reached in the contact algorithm. Generally, it is set as the average side length of the mesh (original mesh element size). The Contact Field defines the maximum permissible penetration as a function of the length of the element size. So it is normally set at 10–20% of the smallest element size in the mesh. In the present study, the smallest element size is set at 0.20 mm, which allows the occurrence of intra-element fracturing.

Static loading is considered for the 2D uniaxial compression test. Displacement controlled loading is imposed on the top loading platen with a constant velocity. Ramp load style is applied with a total displacement of 3.0 mm at the top of the sample when the load factor reaches 1, as is seen in Fig. 5. Note that the bottom platen is fixed in the x and y directions.

4. Results and discussion

4.1. Influence of the height-to-width ratios of the samples on crack initiation, propagation, and coalescence

Three groups of uniaxial compression tests are modeled under static loading condition. Figs. 6–8 present the crack evolution process of the specimens in terms of sample height-to-width ratios (2, 1, and 0.5, respectively). The points a to

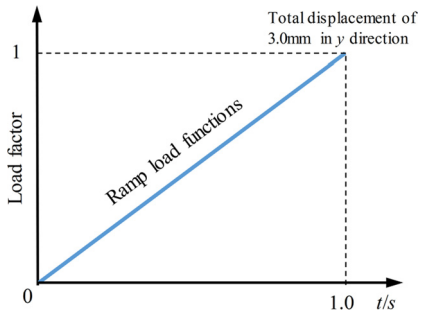

Fig. 5. Loading path under static loading regime.

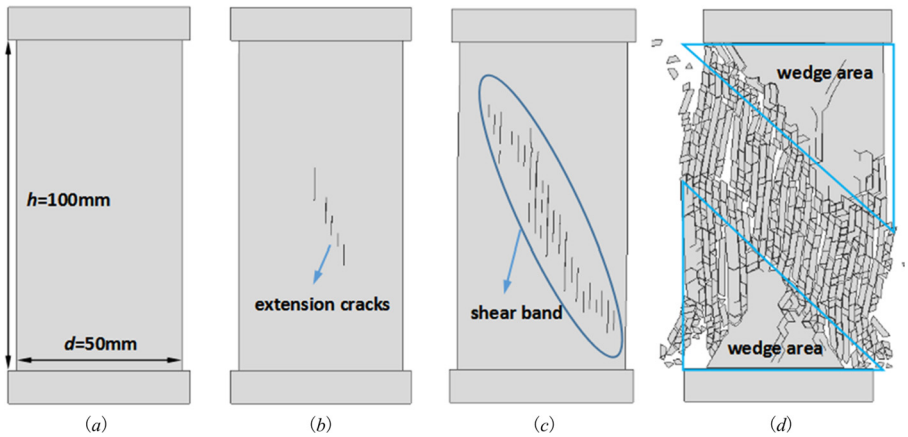

Fig. 6. Crack evolution and failure mode of the specimen when the sample's height-to-width ratio is 2. The letters *a* to *d* correspond to different stages in Fig. 10.

Table 2
Failure evolution stage for corresponding point presented in Fig. 6 to Fig. 8.

Type	Peak Load (N)	*a*		*b*		*c*		*d*	
		Load (N)	(Free of crack)	Load (N)	Crack initiation	Load (N)	Crack propagation or secondary crack initiation	Load (N)	Crack coalescence
$\mu = 2$	9963.9	2977.1	Elastic stage	9281.3	Yield stage	9647.6	Post-peak	2203.6	Post-peak
$\mu = 1$	12486.1	4826.7	Elastic stage	11374.1	Yield stage	10731.8	Yield stage	3281.2	Post-peak
$\mu = 0.5$	7962.3	1252.1	Elastic stage	7952.2	Yield stage	7783.3	Post-peak	2872.1	Post-peak

d in each figure indicate different stages of crack evolution, which represent certain transitional stage from intact rock to fractured rock. Each point that corresponds to the static load and evolution stage is listed in Table 2. It could be seen that point *a*, which shows no cracks in any group, belongs to the elastic stage, while point *b*, representing crack initiation, is in the yield stage, i.e. quite close to the peak load point. The reason for this case is that macroscopic cracks in ELFEN can be obtained only when all the load capacity across the localized failure band decreases to zero, which would lag slightly. Similar situation can also be found in Cai [15] and Hamdi [22]. Points *c* and *d*, representing crack propagation and coalescence in any group, belong to the post-peak stage.

The crack initiation location is of great importance, since it may contribute to various rock and rockmass failure modes. There seems to be an obvious distinction among these three specimens in terms of crack initiation location. For specimens whose sample height-to-width is 2, new cracks are firstly generated in the center of the specimen, and gradually propagate towards the diagonal direction (seen in Fig. 6b and Fig. 6c). However, with the decreasing height-to-width ratio ($\lambda = 1$), new cracks begin to deviate from the central axis and are generated close to one side or both sides of the specimen (seen in Fig. 7b). When the sample's height-to-width ratio is reduced to 0.5, new cracks emerge at the lower boundaries of the specimen, and have a tendency to propagate towards the top and bottom platens as well as to the center of the specimen.

As can be seen in Fig. 6b, the newly generated meso-cracks are basically parallel to the loading direction. Actually, these meso-cracks are all extension cracks in essence. As loading continues, these meso-cracks begin to emerge and propagate towards the diagonal direction in longer specimens. These extension cracks gradually coalesce and subsequently form the

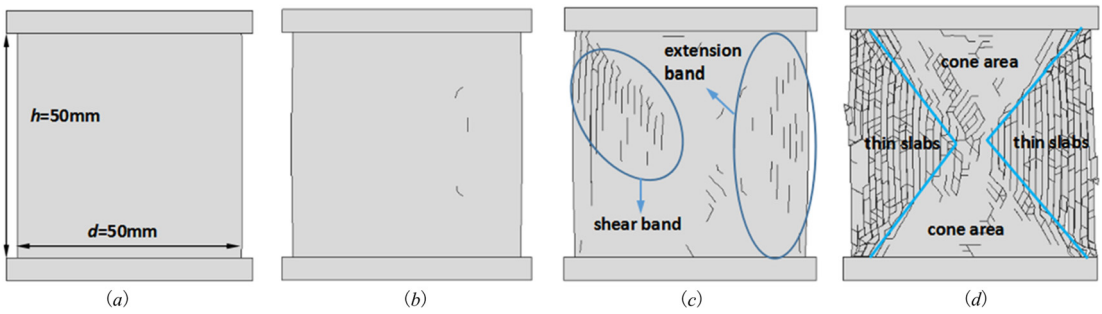

Fig. 7. Crack evolution and failure mode of specimen when the sample's height-to-width ratio is 1. The letters *a* to *d* correspond to different stages in Fig. 11.

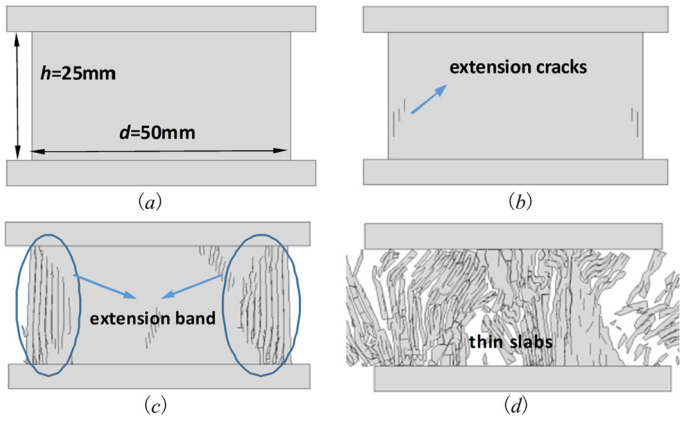

Fig. 8. Crack evolution and failure mode of specimen when sample's height-to-width ratio is 0.5. The letters *a* to *d* correspond to different stages in Fig. 12.

macro shear band, as can be seen in Fig. 6c. The macrocracks finally divide the specimen into two wedge areas, which lead to complete failure. Though some thin slabs could be seen in longer specimen (related to the mesh size), the primary failure mode should be macroscopically shearing. Fig. 7c shows the crack propagation path when $\lambda = 1$ (50 mm × 50 mm). In general, crack propagation and coalescence in such case are accompanied with both the formation of shear and extension bands. The macro shear band then gradually extends and coalesces, and finally forms the opposite vertex cone areas, while the extension bands come into being the splitting areas (seen in Fig. 7d). With further reduction of the sample's height, the final failure mode seems to experience a distinct transformation. When λ is equal to 0.5, the extension bands that are formed by newly generated extension cracks will propagate toward the upper and bottom platens as well as to the central part of the specimen. During the failure process of hard rock, no distinct shear band is formed. The extension bands gradually expand and finally lead to slabbing failure, which is due to many thin slabs, as can be seen in Fig. 8d.

Previous experimental research has shown that the failure modes are related to height-to-width ratios under static loading. Li et al. [6] observed that the macro failure mode will be transformed from shear to slabbing when the height/width ratio is reduced to 0.5 in the prism specimens under uniaxial compression. In their tests, the Iddefjord granite is also selected as typical hard rock to study the failure modes and strength characteristics with a change in the height-to-width ratio. However, very little attention has been paid to the crack initiation location in previous experiments. In the present study, numerical results show that failure modes have experienced shear, tension with shear, and surface-parallel slabbing failure with the decrease in sample height-to-width ratios, and slabbing failure occurs when the ratio is equal to or less than 0.5 in the uniaxial compression test. It seems that the transition of failure mode in previous experimental research is approximately similar to that in the present numerical results. Fig. 9 shows a comparison between the final failure modes in reference [6] and in the present research based on a finite/discrete element approach.

In the early 1960s, people began to concentrate on the axial cleavage failure of rocks under the compression conditions of [4]. In these experiments, the triaxial testing apparatus designed by Brace [7] was used for uniaxial and triaxial compression tests. In uniaxial tests, he found that a large number of microfractures parallel to the loading direction would emerge and propagate along the macro shear band. In the present study, numerical results based on a finite/discrete element approach represent an analogous phenomenon to those observed in previous experimental research. Be carefully observing Figs. 6–8, it could be found out that though macro failure modes are greatly different, the newly generated meso-cracks (initiation cracks) in the specimen should be categorized as extension cracks, which illustrate and validate the essence of extension failure in hard rocks efficiently. With the propagation of cracks, the macro shear band composed of an amount of extension cracks gradually emerges in longer specimens. A relatively longer specimen will prevent the cracks from coalescing along

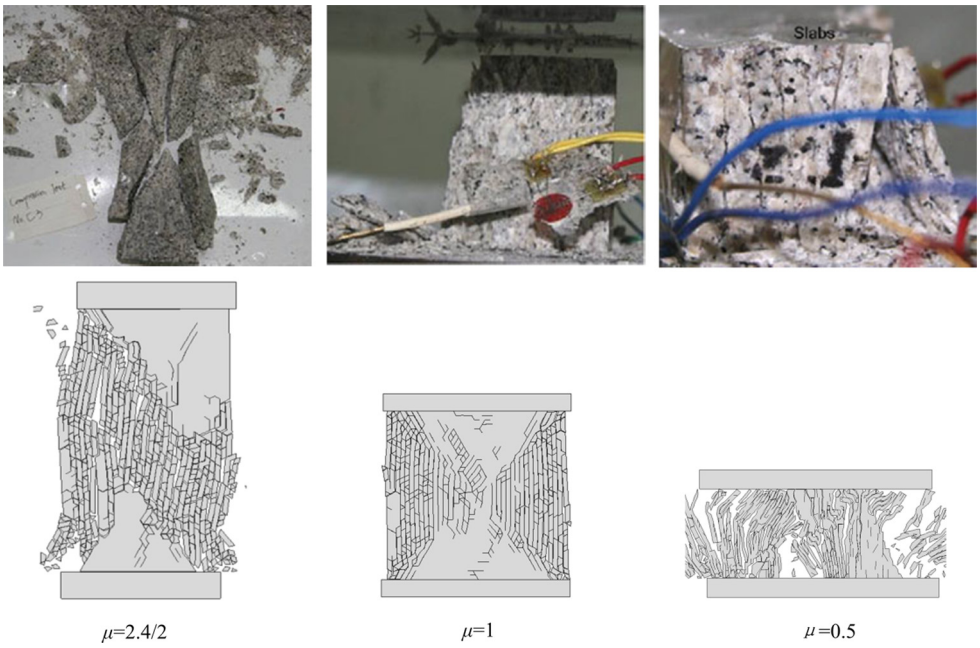

Fig. 9. Comparison of the final failure modes between the results of Li et al. [6] and the present research based on combined FEM/DEM approach.

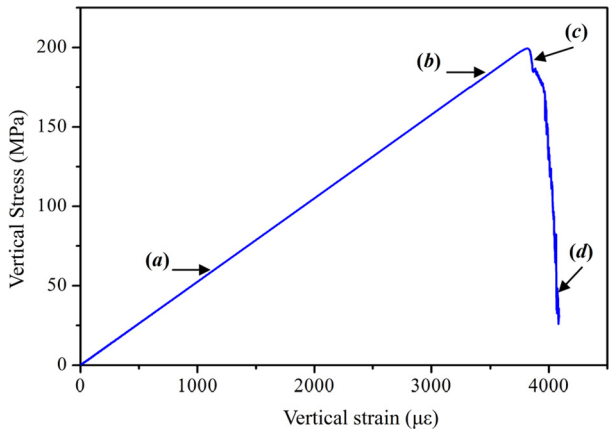

Fig. 10. Stress–strain curve of the specimen when the height-to-width ratio of the sample is 2.

the top and bottom platens, thus a large number of extension bands are suppressed ultimately. With the decrease in the sample's height-to-with ratio ($\lambda = 1$), the macro extension bands begin to emerge near both sides of the specimen, while the central section is still occupied by the opposite vertex cone areas. When the height-to-width ratio of the sample is reduced to 0.5, the final failure mode has turned into slabbing failure. The outcome tends to be the result of the accessible propagation of extension meso-cracks due to short sample height (see Fig. 9).

4.2. Influence of the height-to width ratios of the samples on UCS and slabbing strength

Figs. 10–12 present the stress–strain relation for different sample height-to-width ratios respectively. The points *a* to *d* at each stage in Table 2 are also labeled correspondingly. Note that visible cracks during the failure process could be observed in the yield stage that is close to the peak strength of the hard rock. The post-peak strength in all three curves experiences an abrupt descent that maintains no residual strength. This might be due to the hard and brittle properties for rock materials that distinguish them from ductile materials.

Previous researches have shown that uniaxial and polyaxial compressive strengths are greatly influenced by the slenderness of the rock sample [4,6,7,23,24]. For example, Mogi [4] carried out careful measurements of the apparent compressive strength and fracture angles of Dunham dolomite, Westerly granite, and Mizuho trachyte as functions of the length/diameter ratio, and concluded that the apparent strength decreased markedly with the increase in L/D (length/diameter ratio),

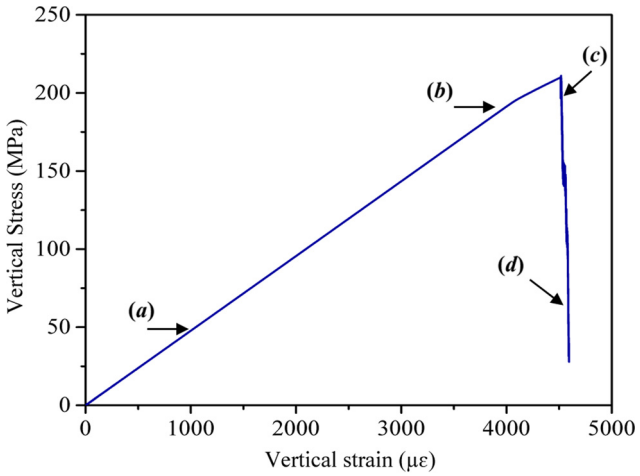

Fig. 11. Stress–strain curve of the specimen when the height-to-width ratio of the sample is 1.

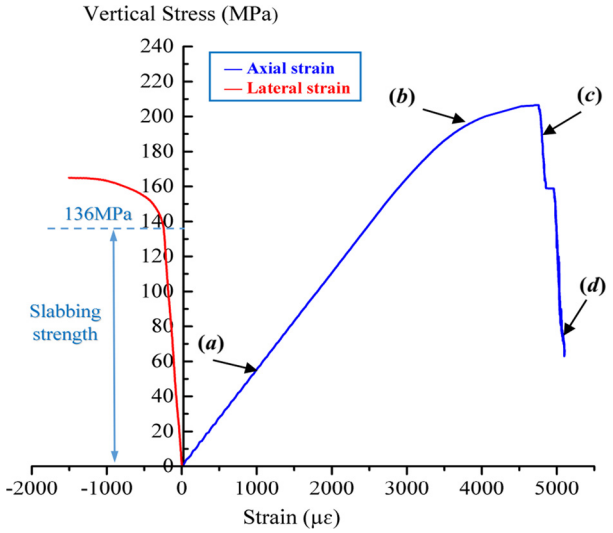

Fig. 12. Stress–strain curve of the specimen when the height-to-width ratio of the sample is 0.5 (including both axial and lateral strain).

but the value becomes nearly constant when L/D is about 2.5. Hudson [23] found that the UCS of the Georgia Cherokee Marble showed an increasing trend with the decrease in the slenderness ratio of the specimen. Zhao and Cai [24] studied the influence of the specimen's height-to-width ratio on the strain-burst characteristics of Tianhu granite under true-triaxial unloading conditions. They found that the peak strength decreases gradually and approached a constant value when the sample's height-to-width ratio increased from 1.0 to 2.5. It is worth noting that the sample's height-to-width ratios are, according to these researchers, greater than or equal to 1, while little attention has been paid to the conditions where they are less than 1. What is more important, though lubricant or other measures were taken in their experiments [7], the end effect cannot be completely eliminated, especially with the decreasing of the specimen's slenderness. In our tests, three types of specimens with height-to-width ratios of 2, 1 and 0.5, respectively, have been pointed out, and the friction between the loading platens and the rock specimen is set to be 0 (see Table 1), where the end effect induced by the end of friction has been eliminated thoroughly. The corresponding peak strength in terms of different sample height-to-width ratios is 199, 211, and 205 MPa, respectively, as can be seen in Figs. 10–12. It can be seen that with the decrease in the slenderness of a rectangular prism specimen, the UCS does not change a lot. In order to illustrate the influence of the end effect on rock strength for different sample height-to-width ratios, the model in which the pre-defined friction between the loading platens and the rock specimen is 0.8 is also simulated to make a comparison with the case when it is 0. The rock's strength is plotted in Fig. 13 for all the cases including the conditions of end friction of 0 and 0.8, and previous experimental results taken from reference [6]. It can be seen from Fig. 13 that the variation trends of the peak strength are extremely distinct with various end friction. The corresponding peak strength in terms of different sample height-to-width ratios for end friction of 0.8 is 202, 252 and 359 MPa respectively, which shows a monotonically increasing trend with the decreasing slenderness. The reason why such results show a higher increase in peak strength as the sample's H/W

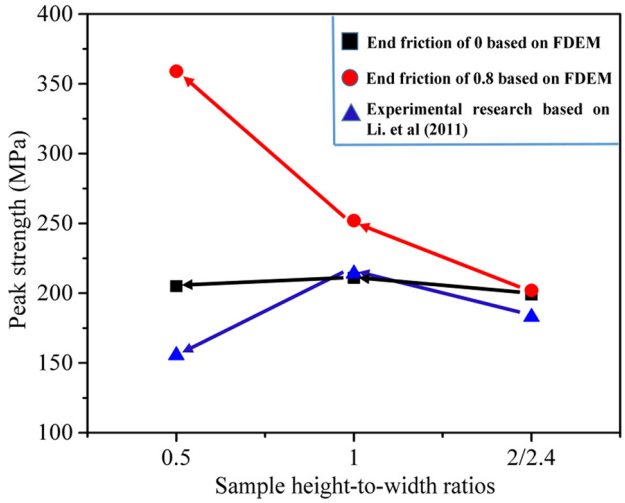

Fig. 13. Variation trend of UCS for different height-to-width ratios based on the present numerical simulation and the results of Li et al. [6].

value decreases should be the additional confinement generated by end friction (thus end effect). On the contrary, if the end effect is completely eliminated from the loading platens, the peak strength will not experience a huge fluctuation or variation for different sample height-to-width ratios any more. In reference [6], Li et al. demonstrated that the increasing trend of the peak strength when the sample's height-to-width ratio decreases from 2 to 1 might be due to the end effects in the specimens. With a further decrease in the sample's height-to-width ratio, the decreasing UCS should be the result of transitional failure modes making that shorter specimens (height-to-width ratio of 0.5) are dominated by slabbing failure (thus extensional fracture instead of shear fracture). In the present study, the failure modes in the Mohr–Coulomb constitutive model with rotating crack are still based on shear fracture or tension cut-off instead of slabbing stress or tensile strain. Therefore, the slabbing fracture mechanism cannot be interpreted completely by using such a constitutive model, which leads to a different strength variation trend, which is to some extent between experimental research and numerical results (end friction of 0). Anyway, the failure modes for previous experimental and current numerical results for different height-to-width ratios are approximately identical.

As described above, the slabbing crack initiation stress obtained in ELFEN software in the present study is not the actual case. Depending on fracture energy, the stages of yielding (initiation of softening) and fracturing (explicit generation of the discrete crack) do not occur simultaneously [15,22]. Another method to obtain the slabbing strength (also deemed as slabbing crack initiation strength) is by means of the lateral strain that departs from its linearity [6]. The stress–lateral strain relation could be observed in Fig. 12 (no stress–lateral strain relation is provided in Fig. 10 and Fig. 11 because it is not necessary to obtain the slabbing strength). In the present study, the corresponding stress when the lateral strain departs from linearity is approximately 136 MPa, so the calculated slabbing strength is about 66% of its uniaxial compressive strength for standard cylindrical specimens. The numerical results based on FDEM are basically consistent with the experimental results by Li et al. [6] (about 60% of the UCS), while they are slightly larger than in site monitoring by Martin [25] (about 56% of the UCS).

4.3. Influence of sample height-to width ratios on the elastic strain energy

The failure process of rock is accompanied with energy dissipation and storage of elastic strain energy [26,27]. The energy dissipation can degrade the rock strength while the release of elastic strain energy would lead to the entire failure of the intact rock. It can be said that the internal impetus of rock fracturing is the release of the stored elastic strain energy, and the failure intensity and destructiveness depends on the amount of elastic strain energy. If the stored elastic strain energy is larger than the surface energy required for the fragmentation of hard rock, then failure would occur, and even result in rock burst induced by abundant kinetic energy. Fig. 14 shows the elastic strain energy distribution versus time for different height-to-width ratios of the sample. Numerical results show that ESE (elastic strain energy) values present the monotonically increasing trend approximately with the passage of time for all the cases, except for $\lambda = 2$ that experiences a slight fluctuation later. Moreover, with the decrease in height-to-width ratios in the sample, the ESE have a tendency to increase at first then to decrease subsequently; the maximum ESE values for the corresponding specimens are 3903 J, 6546 J, and 5094 J, respectively (the samples have failed thoroughly when $t = 0.3$ s for all cases, so the elastic strain energy will not increase afterwards, even if the total loading time is 1 s). Zhao and Cai [24] proposed that strain bursts were more violent for hard rocks with a decrease in H/W (height-to-width ratio), because of the fact that more elastic strain energy had been stored in a shorter specimen, which led to an abrupt and intense release of elastic strain energy when the rock failed. However, their research was merely limited in the condition of $H/W \geq 1$ and the rock specimens were subjected to true-triaxial unloading conditions. In the present study, the ESE value does not present a monotonically increasing trend.

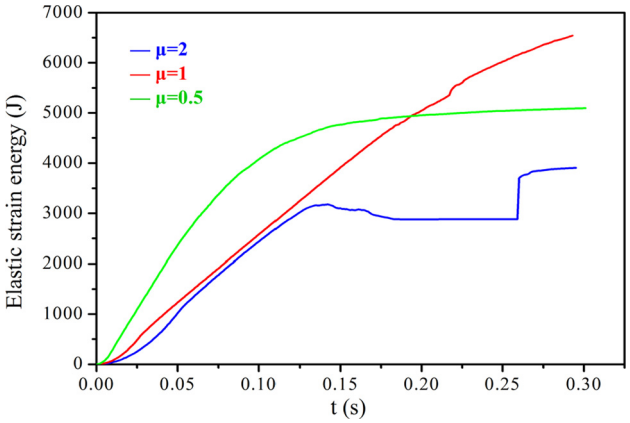

Fig. 14. Elastic strain energy–time relation for different height-to-width ratios of the sample.

Oppositely, the variation curve begins to deviate when the sample's height-to-width ratio is reduced to 0.5, which might be related to transitional failure modes. Fig. 14 shows that the failure intensity or the probability of rock bursts when the height-to-width ratio of the sample is 0.5 is smaller than in the case when $\lambda = 1$, but larger than that the case when $\lambda = 2$. Note that the analysis results are currently only available for uniaxial compressive tests.

In the future, much attention should be paid to such simulations to accurately model the rock specimen in true triaxial loading and unloading tests influenced by the height-to-width ratios of the sample. In addition, 3D models will be used for a better illustration of failure modes and strength criteria of hard and brittle rocks.

5. Conclusions

The finite/discrete element approach is adopted to model the failure process of rectangular prism specimens under uniaxial compression tests. The main purpose of the paper is to investigate the influence of the height-to-width ratios of the samples (2, 1 and 0.5 respectively) on the failure modes and strength characteristics of typical hard and brittle rocks named Iddefjord granite.

Numerical modeling indicates that the crack initiation location will shift from the center to both sides of the specimen when decreasing the height-to-width ratio. The failure modes have experienced the shear, tension with shear and surface-parallel slabbing failure with the decrease in height-to-width ratios, and slabbing failure takes place when the ratio is equal to or less than 0.5 in the uniaxial compression test. The numerical results illustrate and validate the essence of extension failure in hard rocks whatever the failure modes. It seems the macro shear band in longer specimen is composed of meso-extension cracks while slabbing failure might be due to the accessible propagation of extension meso-cracks for short sample height under uniaxial compression test. The UCS of rectangular prism specimen for three types of rock sizes does not change a lot if end effect between the loading platens and rock specimen is eliminated completely. The end effect is also considered to investigate the UCS of hard rocks for all cases. The corresponding slabbing strength in which the lateral strain departs from linearity when $\lambda = 0.5$ is approximately 136 MPa, with a calculation of 66% of its uniaxial compressive strength for standard cylindrical specimens. In addition, the maximum elastic strain energy stored in rock specimen experience the tendency of a first increase then a decrease, indicating a higher failure intensity and degree for $\lambda = 1$.

Acknowledgements

The authors would like to acknowledge the financial supports from the State Key Research Development Program of China [grant number 2016YFC0600706], the National Natural Science Foundation of China [grant numbers 11472311, 51474250], and the Fundamental Research Funds for the Central Universities of Central South University [grant number 2016zzts097]. The authors also express their acknowledgments to the anonymous reviewers for their precious comments.

References

[1] H. Zhou, J.J. Lu, R.C. Xu, Critical problems of study of slabbing failure of surrounding rock in deep hard rock tunnel and research progress, Rock Soil Mech. 36 (10) (2015) 2737–2749.
[2] J.M. Ramsey, F.M. Chester, Hybrid fracture and the transition from extension fracture to shear fracture, Nature 428 (2004) 63–66.
[3] K. Du, M. Tao, X.B. Li, J. Zhou, Experimental study of slabbing and rockburst induced by true-triaxial unloading and local dynamic disturbance, Rock Mech. Rock Eng. 49 (9) (2016) 3437–3453.
[4] K. Mogi, Experimental Rock Mechanics, CRC Press, Boca Raton, FL, USA, 2007.
[5] J. Gramberg, The axial cleavage fracture 1: axial cleavage fracturing, a significant process in mining and geology, Eng. Geol. 1 (1) (1965) 31–72.
[6] D.Y. Li, C.C. Li, X.B. Li, Influence of sample height-to-width ratios on failure mode for rectangular prism samples of hard rock loaded in uniaxial compression, Rock Mech. Rock Eng. 44 (3) (2011) 253–267.

[7] W.F. Brace, Brittle fracture of rocks, in: W.R. Judd (Ed.), State of Stress in the Earth's Crust, Elsevier, New York, 1964, pp. 111–174.
[8] W.R. Wawersik, C. Fairhurst, Study of brittle rock fracture in laboratory compression experiments, Int. J. Rock Mech. Min. Sci. Geomech. Abstr. 7 (5) (1970) 561–575.
[9] A. Fakhimi, B. Hemami, Axial splitting of rocks under uniaxial compression, Int. J. Rock Mech. Min. Sci. 79 (2015) 124–134.
[10] F. Freddi, G. Royer-Carfagni, Variational fracture mechanics to model compressive splitting of masonry-like materials, Ann. Solid Struct. Mech. 2 (2011) 57–67.
[11] Z.J. Wen, X. Wang, L.J. Chen, G. Lin, H.L. Zhang, Size effect on acoustic emission characteristics of coal-rock damage evolution, Adv. Mater. Sci. Eng. 2017 (2017) 1–8.
[12] W.D. Ortlepp, The behaviour of tunnels at great depth under large static and dynamic pressures, Tunn. Undergr. Space Technol. 16 (1) (2001) 41–48.
[13] C.D. Martin, W.G. Maybee, The strength of hard-rock pillars, Int. J. Rock Mech. Min. Sci. 37 (8) (2000) 1239–1246.
[14] Z. Wu, L.N.Y. Wong, Frictional crack initiation and propagation analysis using the numerical manifold method, Comput. Geotech. 39 (1) (2012) 38–53.
[15] M. Cai, Fracture initiation and propagation in a Brazilian disc with a plane interface: a numerical study, Rock Mech. Rock Eng. 46 (2) (2013) 289–302.
[16] D. Elmo, D. Stead, E. Eberhardt, A. Vyazmensky, Applications of finite/discrete element modeling to rock engineering problems, Int. J. Geomech. 13 (5) (2013) 565–580.
[17] A. Munjiza, D.R.J. Owen, N. Bicanic, A combined finite-discrete element method in transient dynamics of fracturing solids, Int. J. Eng. Comput. 12 (2) (1995) 147–174.
[18] M. Cai, Influence of intermediate principal stress on rock fracturing and strength near excavation boundaries-insight from numerical modeling, Int. J. Rock Mech. Min. Sci. 45 (5) (2008) 763–772.
[19] B. Paul, A modification of the Coulomb–Mohr theory of fracture, J. Appl. Mech. 28 (2) (1961) 259–268.
[20] P.A. Klerck, The Finite Element Modelling of Discrete Fracture in Quasi-Brittle Materials, University of Wales, Swansea, Wales, 2000.
[21] Rockfield, Rockfield Software Ltd, Technium, Kings Road, Prince of Wales Dock, Swansea, SA1 8PH, UK, 2013.
[22] P. Hamdi, D. Stead, D. Elmo, Damage characterization during laboratory strength testing: a 3D-finite-discrete element approach, Comput. Geotech. 60 (7) (2014) 33–46.
[23] J.A. Hudson, S.L. Crouch, C. Fairhurst, Soft, stiff and servo-controlled testing machines: a review with reference to rock failure, Eng. Geol. 6 (3) (1972) 155–189.
[24] X.G. Zhao, M. Cai, Influence of specimen height-to-width ratio on the strainburst characteristics of Tianhu granite under true-triaxial unloading conditions, Can. Geotech. J. 52 (7) (2014) 890–902.
[25] C.D. Martin, Seventeenth Canadian geotechnical colloquium: the effect of cohesion loss and stress path on brittle rock strength, Can. Geotech. J. 34 (5) (1997) 698–725.
[26] H.P. Xie, Y. Ju, L.Y. Li, Criteria for strength and structural failure of rocks based on energy dissipation and energy release principles, Chin. J. Rock Mech. Eng. 24 (17) (2005) 3003–3010.
[27] J.Q. Guo, Q. Zhao, J.B. Zhang, J. Zhang, Rockburst prediction based on elastic strain energy, Chin. J. Rock Mech. Eng. 34 (9) (2015) 1886–1893.